ELSEVIER

Contents lists available at ScienceDirect

Journal of the European Ceramic Society

journal homepage: www.elsevier.com/locate/jeurceramsoc





Microstructural and compositional design of Cr₂AlC MAX phases and their impact on oxidation resistance

Clio Azina ^{a,*}, Melina Poll ^b, Damian M. Holzapfel ^a, Elodie Tailleur ^c, Axel Zuber ^d, Sylvain Dubois ^d, Per Eklund ^e, Jesus Gonzalez-Julian ^{b,f}

- ^a Materials Chemistry, RWTH Aachen University, Kopernikusstraße 10, Aachen D-52074, Germany
- b Forschungszentrum Jülich GmbH, Institute of Energy and Climate Research: Materials Synthesis and Processing (IEK-1), Jülich 52425, Germany
- ^c CRM2-University of Lorraine, Vandoeuvre-Lès-Nancy, France
- ^d Institut PPRIME, CNRS/Université de Poitiers/ENSMA, UPR 3346, TSA 41126, Poitiers Cedex 9 86073, France
- e Thin Film Physics Division, Department of Physics, Chemistry, and Biology (IFM), Linköping University, Linköping SE-581 83, Sweden
- f Chair of Ceramics, Institute of Mineral Engineering (GHI), RWTH Aachen University, Forckenbeckstrasse 33, Aachen 52074, Germany

ARTICLE INFO

Keywords: MAX phases Reactive sintering Microstructural design Oxidation

ABSTRACT

The oxidation of MAX phases has largely been investigated, but the effect of secondary phases and microstructure is still unclear. We report on the effect of reactive and non-reactive sintering, and starting powders, on the microstructure, phase formation, and chemical composition of Cr_2AlC MAX phases. The grain sizes are shown to be sensitive to both the processing method and the starting powders. Secondary phases were observed mostly in reactively sintered samples as Cr_7C_3 and $AlCr_2$ were identified, and Al contents varied between 24.4 and 28.0 at %. Finally, the oxidation behavior of the produced MAX phases was evaluated after 60 and 120 min at 1100 °C. The Al content, the average grain size of the as-sintered samples, and the presence of secondary phases affected the decomposition of the MAX phase into Cr-carbides in the vicinity of the oxide scale and the composition of the oxide scale, respectively.

1. Introduction

MAX phases constitute a family of inherently nanolaminated carbides and nitrides that are given by the formula $M_{n+1}AX_n$, where M is a transition metal, A is an A-group element, and X is either carbon and/or nitrogen (n=1, 2, 3) [1,2]. All the MAX phase compositions crystallize in a hexagonal $P6_3/mmc$ structure, which, combined with the chemical composition, provide them with a unique combination of metallic and ceramic properties [3]. MAX phases are promising for a variety of applications, particularly those that operate in aggressive environments and/or high temperature [4–10].

Aside from good thermal and chemical stability, certain MAX phase compositions are characterized by excellent high-temperature oxidation resistance. In particular, Al-containing MAX phases such as Ti_2AlC [5, 11] and Cr_2AlC [12–14] exhibit very good oxidation resistance because of the formation of a protective scale at the surface of the MAX phase. Indeed, the weakly bonded Al tends to diffuse to the surface and react with the oxidizing environment to form Al_2O_3 . The presence of this oxide scale allows decreasing the inward diffusion of oxygen species

and, therefore, increases the lifetime of the MAX phase in aggressive conditions. In the case of $\rm Cr_2AlC$, in particular, the outward $\rm Al^{3+}$ diffusion leads to the Al-depletion of the MAX phase in the vicinity of the newly formed oxide scale and eventually to the transformation of the Al-depleted MAX phase into Cr-carbides ($\rm Cr_3C_2$ and $\rm Cr_7C_3$). As oxidation progresses further, the Cr-carbide formed oxidizes as well and releases volatile species – mostly CO and $\rm CO_2$ - causing pore formation, which is detrimental for the mechanical integrity of the MAX phase. Therefore, efforts have been concentrated on limiting the outward Al diffusion in order to avoid the formation of Cr-carbides during oxidation.

As the microstructure is one of the major factors influencing oxidation, because of grain boundary diffusion of oxidizing and material species, different strategies were employed to tune the microstructures of bulk and thin film MAX phases. Shang $\it et al.$ investigated the oxidation behavior of $\rm Cr_2Al_{1-x}Si_xC$ (0<x<0.07) thin films and reported the effect Si had on the microstructure of the MAX phase [15]. In comparison with pure $\rm Cr_2AlC$, Si hindered grain growth upon oxidation of the MAX phase and led to thicker oxide scales after oxidation at 1120 °C for 4 h. This behavior was further described by Pradeep $\it et al.$ who reported the

E-mail address: azina@mch.rwth-aachen.de (C. Azina).

^{*} Corresponding author.

formation of Cr₃Si precipitates at the column boundaries of the MAX phase which inhibited grain growth [16].

Li *et al.* reported differences between the oxidation behavior of fine-grained (2 μ m) and coarse-grained (60 μ m) Cr_2AlC and stated that for long oxidation times fine-grained Cr_2AlC did not form Cr_7C_3 due to the enhanced Al diffusion at the grain boundaries [17]. More recently, Zuber *et al.* reported the oxidation behavior of fine (2 μ m) and coarse-grained (50–100 μ m), produced by HIP and spark plasma sintering (SPS), and single crystal Cr_2AlC [18]. Al_2O_3 and Cr_7C_3 were observed in both HIP and SPS samples, leading to the assumption that the microstructure does not have that strong of an effect on the oxidation behavior of Cr_2AlC . Furthermore, oxidation carried out with wet and dry air showed that while the oxidation products are the same for both fine-and coarse-grained Cr_2AlC , the fine-grained MAX phase oxidizes faster [12].

Microstructural design of bulk materials, including MAX phases, is often achieved by using different processing methods such as HIP and SPS, and by tuning the processing parameters such as heating rate and dwell time, to name a few. Herein, we explore a different method to design Cr_2AlC microstructures based on the nature and size of the starting powder precursors. We discuss the phase formation and grain size of Cr_2AlC samples obtained by either sintering of MAX phase powders or by reactive sintering of elemental powders. The different microstructures are then evaluated with respect to their oxidation behavior in order to deduce whether fine-grained microstructures behave differently than coarse-grained ones. We also discuss the effects of chemical composition and secondary phases, which are different based on the processing route, on the oxidation resistance of the MAX phase.

2. Methods

Three different synthesis routes were selected to produce dense Cr_2AlC with different microstructures. Solid State Reaction (SSR) and Molten Salt Shielded Synthesis (MS3) are two-step processes where the powders are synthesized first, followed by a sintering process. The third synthesis route, Reactive Sintering (RS), allows for the production of dense Cr_2AlC in just a single step, as the synthesis and sintering take place simultaneously.

2.1. Solid state reaction

SSR is extensively used to synthesize MAX phases due to the high purity of the resulting powders. The detailed information on the process can be found elsewhere [19]. Cr ($d_{50}=28.0~\mu m,~99.0\%,$ Alfa Aesar), Al ($d_{50}=9.1~\mu m,~99.5\%,$ Alfa Aesar) and graphite ($d_{50}=6.9~\mu m,~99.0\%,$ Alfa Aesar) powders were mixed in a molar ratio of 2:1.1:0.97, respectively. An excess of 10 at% in Al was added to compensate for Al loss during heating. The mixture was compacted and heated up to $1350~^{\circ} C$ in Ar atmosphere for 3 h. The heating and cooling rates were $10~^{\circ} C/min.$ The resulting Cr₂AlC porous sample was ground using planetary milling at 250 RPM for 2 h using zirconia balls of 5 mm in diameter, in ethanol. After drying, the powder was passed through a 63 μm sieve.

2.2. Molten salt shielded synthesis

The MS3 method was developed recently to produce non-oxide ceramics, such as MAX phases, in air at relatively low temperatures [20]. Cr ($d_{50}=28.0~\mu m,~99.0\%$, Alfa Aesar), Al (-325~m esh,~99.5%, Alfa Aesar) and graphite (APS 7–11 $\mu m,~99.0\%$, Alfa Aesar) were mixed in a 2:1.25:0.9 molar ratio, respectively. KBr salt (99.0%, Alfa Aesar) was mixed with the starting precursors in a 1:1 weight ratio. The raw materials were mixed in ethanol using zirconia balls of 5 μm in diameter, in a 3D shaker/mixer (Manufacturer: Turbula) for 24 h. The mixture was then dried in a rotary evaporator at 70 °C, followed by sieving through a 300 μm sieve. The dried mixture was compacted into 20 mm-diameter

pellets at 200 MPa with a uniaxial hand press. The pellets were placed in a cylindrical alumina crucible, which was subsequently filled with KBr. The alumina crucibles were introduced in a high-temperature furnace and heated in air at a rate of 5 °C/min, up to 1150 °C and kept there for 3 h. After cooling, the crucible was washed with hot water to remove the KBr. Vacuum filtration of the MAX phase powder was carried out with boiling deionized water and ethanol to further reduce the salt content. Finally, the powder was dried at 70 °C and passed through a 25 μ m sieve.

Once the SSR and MS3 powders were synthesized, the next step was the densification using, in this case, a Field Assisted Sintering Technology/Spark Plasma Sintering (FAST/SPS, FCT-HPD5, FCT Systeme GmbH, Germany). 10.5 g of powders were poured into a 30 mm inner diameter graphite tool, which was covered with a graphite felt to reduce heat loss. The thermal cycle was carried out under vacuum (~4 mbar). The maximal temperature of 1200 °C was reached with a heating rate of 100 K·min⁻¹ and was kept for a dwell time of 10 min while applying a uniaxial pressure of 50 MPa. The temperature was controlled using a pyrometer that was focused on the surface of a drilled punch at only 5 mm from the powder. After the densification process, the sample surfaces were ground and polished to eliminate the remaining graphite.

2.3. Reactive sintering

Elemental powders were also used to produce Cr_2AlC pellets in one step. Similar to the SSR powder preparation, Cr ($d_{50}=28.0~\mu m,\, 99.0\%$, Alfa Aesar), Al ($d_{50}=9.1~\mu m,\, 99.5\%$, Alfa Aesar) and carbon-source powders were mixed together in a molar ratio in Cr, Al, and C of 2:1.02:0.97, respectively. The carbon sources used were graphite ($d_{50}=6.9~\mu m,\, 99.0\%$, Alfa Aesar), carbon black (nanoscale powderagglomerate $d_{50}=8.17~\mu m,\, >99.9\%$, Alfa Aesar), and Cr_3C_2 ($d_{50}=6.0~\mu m,\, 99.5\%$, Alfa Aesar) which are expected to have an effect on the grain size of the sintered MAX phase. Indeed, carbon black has a substantially smaller size than graphite, and Cr_3C_2 is expected to lead to a coarser microstructure than graphite. In the following sections, the samples sintered with graphite, carbon black, and Cr_3C_2 powders will be referred to as RS, RS.cb, and RS. Cr_3C_2 , respectively.

The powder mixtures were placed in a graphite mold of 30 mm in diameter, and the sintering program used involved heating up to 1200 $^{\circ}\text{C}$ with a heating rate of 20 $^{\circ}\text{C/min}$, a hold time of 15 min, and 30 MPa of pressure.

The final pellets obtained by the three different routes were polished and cut into approx. $10\times10~\text{mm}^2$ specimens of approx. 2 mm in thickness.

The chemical compositions of the sintered specimens were measured in a JEOL JSM 6480 scanning electron microscope (SEM) equipped with an EDAX Genesis 2000 energy dispersive x-ray spectroscopy detector (EDX). Each measurement was carried out with an acceleration voltage of 12 kV, and each spectrum was quantified based on a reference sample that had previously been measured using elastic recoil detection analysis (ERDA).

X-ray powder diffraction (XRD) experiments were performed on a PANalytical X'PertPRO diffractometer with Cu $K_{\alpha 1}$ radiation ($\lambda{=}1.5406$ Å) in Bragg-Brentano geometry. Data collection was carried out in the scattering angle range of $5{-}150^\circ$ with a 0.0167° step size. The exposure time was adjusted for each sample in order to obtain a good signal to noise ratio. Rietveld refinements were performed with the FullProf software [21]. The unit-cell parameters as well as the scale factors for the Cr2AlC and secondary phases were refined, while the atomic positions of the secondary phases were not. Finally, the peaks' profile was fitted using a Thompson-Cox-Hastings Pseudo-Voigt function.

The grain size distributions and orientations of the samples were investigated using Electron Backscattered Diffraction (EBSD) in a Helios NanoLab G3 CX DualBeam SEM equipped with a FEG ELSTAR electronic column and an EDAX TEAM Pegasus microanalysis set including a HIKARI Super EBSD camera. Prior to the measurements, the samples were first polished with silicon carbide discs, then diamond suspensions

Table 1Starting powders, sintering parameters, and relative densities of the samples produced.

Sample ID	Precursors	Sintering Temperature (°C)	Pressure (MPa)	Heating Rate (°C/min)	Hold Time (min)	Relative Density (%)
SSR	Cr ₂ AlC (SSR)	1200	50	100	10	98.3
MS^3	Cr ₂ AlC (MS3)	1200	50	100	10	96.5
RS	Cr+Al+C ^a	1200	30	20	15	99.2
RS.cb	Cr+Al+cb ^b	1200	30	20	15	99.9
RS.Cr ₃ C ₂	$Cr+Al+Cr_3C_2$	1200	30	20	15	99.9

a C: graphite.

b cb: carbon black

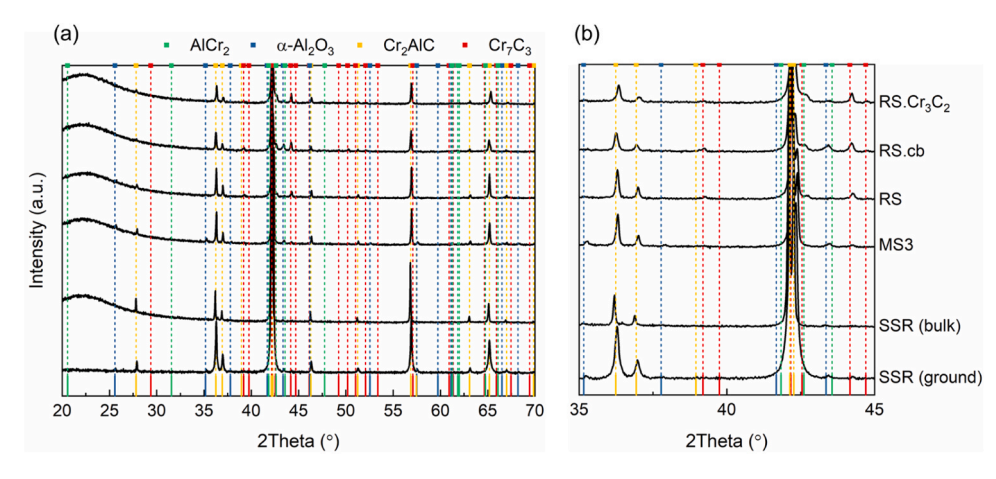


Fig. 1. (a) XRD patterns of as-sintered Cr_2AlC samples. (b) Magnification of the 35–45° 2θ region. PDF cards: $AlCr_2 - ICSD$ 57651, α - $Al_2O_3 - ICDD$: 00–046-1212, $Cr_2AlC - ICSD$: 1252614, $Cr_7C_3 - ICDD$: 00–036-1482.

on felt disc before being chemo-mechanically polished with a colloidal alumina suspension. The orientation maps were acquired using the Pattern Region of Interest Analysis System (PRIAS) software (EDAX TEAM version 4.5.0.0.), and the microstructure analysis and Inverse Pole Figure maps plotted with OIM Analysis software (version 7.3.0.3.).

The oxidation was monitored by differential scanning calorimetry (DSC, Netzsch Jupiter® STA 449 C). A small 5×5 mm² MS3 specimen was prepared from cutting a larger specimen. The DSC measurement was performed in air in continuous heating mode. The sample was preheated to $150~^{\circ}\text{C}$ to allow for degassing and was then heated to $1100~^{\circ}\text{C}$ with a heating rate of 20~K/min.

Additional oxidation experiments were carried out on specimens of $10\times10\times2~\text{mm}^3,$ in an open furnace. The oxidation temperature was set to $1100~^\circ\text{C},$ and the samples were inserted into the furnace at once. Once the samples had reached $1100~^\circ\text{C},$ the timer was set for 60 and 120 min. The samples were removed from the furnace gradually and allowed to cool down naturally.

The phase identification post-oxidation was carried out using a Siemens D5000 system with Cu radiation, in Bragg-Brentano configuration, using Cu $K_{\alpha 1}$ radiation ($\lambda{=}1.5406\,\text{Å})$ in the range of 5–70°, with a step size of 0.05°.

Finally, thin lamellae were extracted from the oxidized samples using a focused ion beam (FEI Helios Nanolab 660) equipped with a scanning transmission electron microscopy detector (STEM III). Imaging was carried out in high-angle annular dark field (HAADF) and bright field (BF). Cross-section EDX line scans were carried out using an EDAX system with an Octane Elect detector using an acceleration voltage of 12 kV, a current of 1.6 nA and a step size of 50 nm.

3. Results and discussion

Table 1 gathers the sintering parameters of each processing route and the resulting relative densities of the samples produced. The heating rate was decreased from 100 to 20 K/min for the reactively sintered samples

 Table 2

 Secondary phase contents extracted from Rietveld refinements.

Sample	Cr ₂ AlC (wt%)	Cr ₇ C ₃ (wt%)	Al ₂ O ₃ (wt%)	AlCr ₂ (wt%)	Bragg R- factor	χ ²
SSR	~90	<3	<3	<3	16.03	2.14
MS^3	86.2	~1	12.8	-	7.79	1.38
RS	93.7	7.3	-	-	9.022	1.36
RS.cb	81.9	11.1	-	7	7.196	1.29
RS.	84.5	11.6	-	3.9	11.16	1.46
Cr_3C_2						

to allow for the reaction to be completed. While all samples were dense (> 96 %), the highest values correspond to the reactively sintered samples. We explain these small differences by the possible presence of a native oxide scale surrounding the SSR and MS3 $\rm Cr_2AlC$ powders, which were prepared prior to sintering/consolidation. Furthermore, the irregular shapes of the synthesized MAX phase powders could also be responsible for lower green density and presence of larger pores.

The XRD patterns of the as-sintered Cr_2AlC samples are provided in Fig. 1. All samples exhibit MAX phase peaks which are indicated by the yellow lines. The SSR sample was measured in as-sintered form but also after grinding the specimen down to a powder in order to remove any potential texture effects caused by the very intense 002 peak at $\sim 13^\circ$. In fact, such texturing can be expected considering that the powders are anisotropic and can be aligned during sintering. The secondary phases identified were Al_2O_3 , Cr_7C_3 , and $AlCr_2$, which are shown by the blue, red, and green lines, respectively. Based on Rietveld refinements, the most common secondary phase was Cr_7C_3 , which is a common secondary phase found in sintered Cr_2AlC . In addition to the carbide phase, the SSR, RS.cb, and RS. Cr_3C_2 samples also exhibited peaks corresponding to $AlCr_2$, while MS3 and SSR also showed the presence of Al_2O_3 .

Rietveld refinements were carried out to identify the secondary phases formed in each sample and extract their fractions, which are given in Table 2. Secondary phases could only be identified in the

 $\begin{tabular}{ll} \textbf{Table 3} \\ \textbf{Chemical compositions of sintered Cr_2AlC samples obtained by $ERDA$-corrected EDX.} \end{tabular}$

Sample ID	C at%	O at%	Al at%	Cr at%	Cr/Al ratio
SSR	18.4 ± 0.6	0.9 ± 0.1	25.5 ± 0.2	55.2 ± 0.6	2.16/1.00
MS^3	24.0 ± 1.8	0.7 ± 0.1	28.1 ± 0.8	47.3 ± 1.0	1.69/1.00
RS	23.5 ± 0.5	0.6 ± 0.1	24.4 ± 1.1	51.6 ± 0.5	2.11/1.00
RS.cb	24.9 ± 1.4	0.6 ± 0.1	27.2 ± 0.5	47.2 ± 1.0	1.73/1.00
RS.Cr ₃ C ₂	23.1 ± 0.4	0.4 ± 0.1	25.3 ± 0.2	51.2 ± 0.3	2.02/1.00

ground SSR sample shown in Fig. 1. However, the exact phase fractions could not be extracted because of low intensities. Therefore, we suggest that the overall secondary phases amount to less than 3 wt% for each phase independently. The reactively sintered samples contained between 7.3 and 11.6 wt% of $\rm Cr_7C_3$, while the RS.cb and RS.Cr_3C_2 samples also showed up to 7 wt% of AlCr_2, indicating that the reaction was not completed during sintering. The MS3 sample contained traces of $\rm Cr_7C_3$ (~1 wt%), and nearly 13 wt% of Al_2O_3. The presence of Al_2O_3 is directly linked to the MS3 process, which takes place in ambient air. Overall, the most secondary phases were detected in the RS.cb sample, which were mostly due to an incomplete reaction.

The chemical compositions of the sintered Cr₂AlC samples, measured against an ERDA standard are provided in Table 3. All samples possess a

stoichiometry close to the 2:1:1 expected for the Cr_2AlC MAX phase, although some deviations can be observed. For example, the SSR sample is particularly carbon-deficient. Furthermore, the Cr to Al ratios are also fairly different within the sample set. In fact, the most stoichiometric sample is $RS.Cr_3C_2$, while RS.cb and RS samples are slightly overstoichiometric in Al, and the SSR and RS samples are slightly overstoichiometric in RS. These differences might play an important role in the oxidation behavior of the samples.

The microstructure and, therefore, grain size distributions resulting from sintering the different precursors were investigated using EBSD, and the corresponding maps are provided in Fig. 2. While the 002 peak observed for the bulk SSR sample in Fig. 1 hinted at a certain degree of texture, the EBSD map in Fig. 2(a) shows that there is no preferential orientation at this observation scale. Each precursor led to different grain size distributions, with the most coarse-grained sample being the RS.Cr₃C₂ sample, with an average grain size of approx. 9 μ m. The SSR sample averaged at approx. 5 μ m, followed by the MS3 and RS samples at approx. 4 and 3 μ m, respectively. Finally, as expected, the most finegrained sample was the RS.cb sample (approx. 2 μ m). Sub-micron grains can be seen in the MS3 and RS.cb maps in Fig. 2(b) and (d), indicating that there are at least two grain size populations in these samples. This can be expected for both the MS3 and RS.cb samples for two separate reasons. In the case of MS3, the powder synthesis is driven by

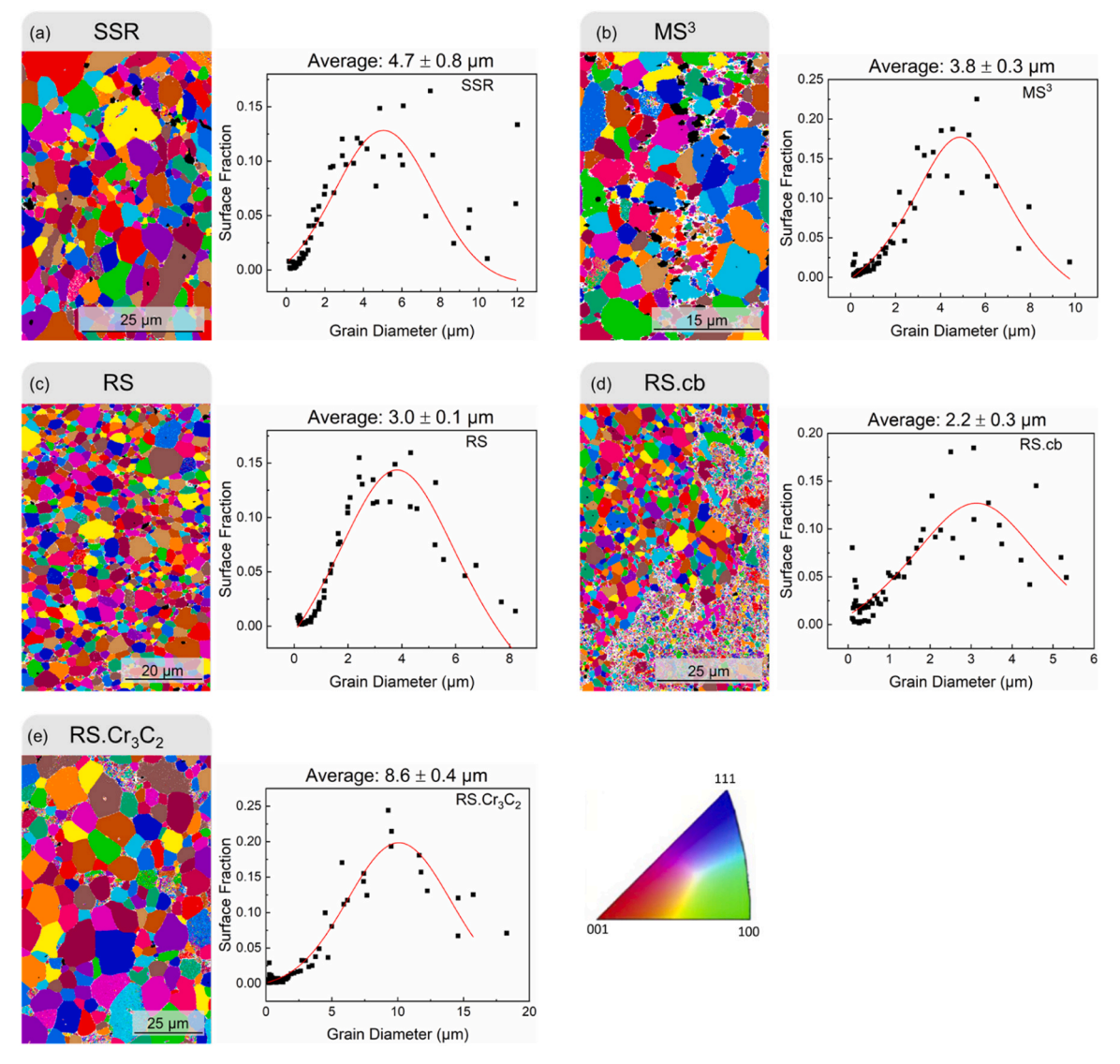


Fig. 2. EBSD maps of Cr₂AlC samples processed with different starting powders and corresponding grain size distributions.

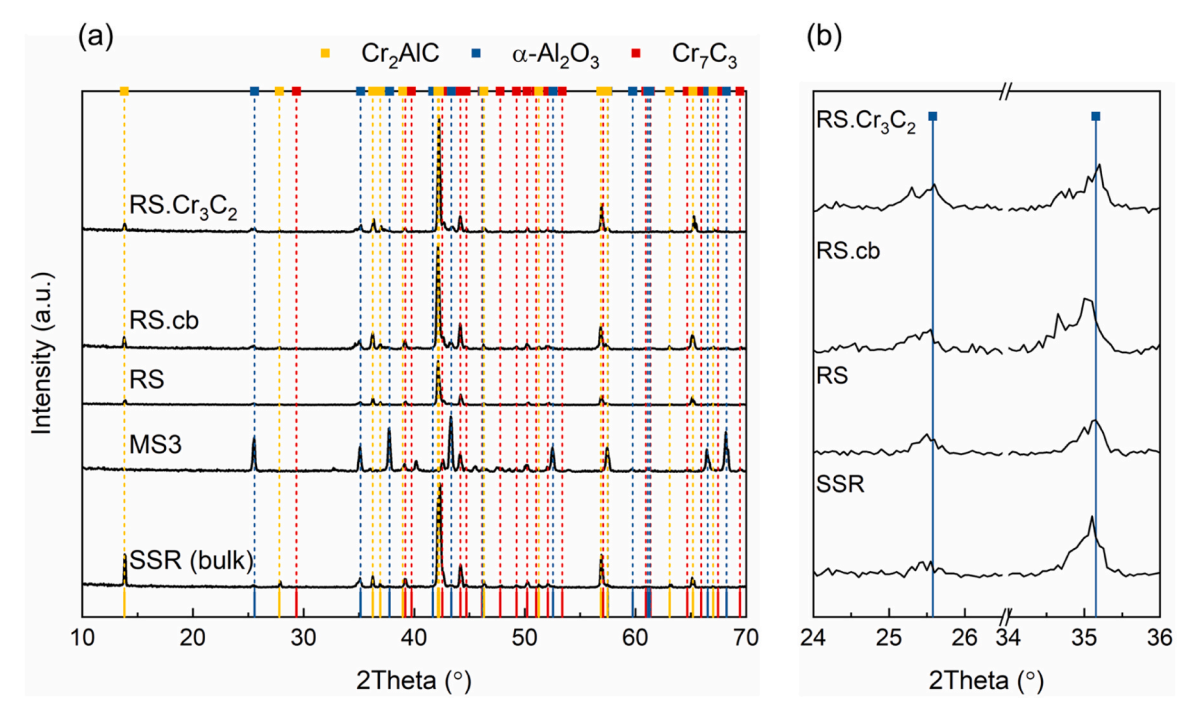


Fig. 3. (a) XRD patterns of Cr_2AlC samples after 60 min oxidation at 1100 °C, in air. (b) magnification of the 24-36° 2θ range with α - Al_2O_3 indices (MS3 was excluded because of its poor oxidation performance). PDF cards: $Cr_2AlC - 00-029-0017$, α - $Al_2O_3 - 00-046-1212$, $Cr_7C_3 - 00-036-1482$.

dissolution-precipitation and hence nucleation can occur spontaneously leading to the formation of smaller grains [20,22]. In the case of RS.cb, Cr and Al have higher diffusivities than carbon, therefore, the carbon powders will act as nucleation sites for metal species to diffuse to. Considering the nanometric size of carbon black, smaller grain sizes are also expected for this sample. Furthermore, the short duration of the SPS processes (10 min for MS3 and 15 min for RS.cb) allowed limiting, and even inhibiting, grain growth which led to microstructures that have not fully evolved. In contrast, the larger grain sizes obtained in the case of RS.Cr₃C₂ are most likely due to the large Cr_3C_2 powder grains, which acted as carbon sources.

The samples were then oxidized at 1100 °C, in air for 60 min. The XRD patterns of the oxidized samples are shown in Fig. 3. The MAX phase peaks can be observed in all XRD patterns except that of the MS3 sample. In fact, based on the pattern shown herein, the MAX phase has either been fully consumed and transformed into the oxide scale (Al₂O₃) and carbides, or the scale formed is thick enough that the underlying MAX phase is not detected by XRD. The remaining samples exhibited peaks corresponding to Al₂O₃ and Cr₇C₃ which are usual oxidation products formed during high temperature oxidation of Cr2AlC. Indeed, the Al from the MAX phase tends to diffuse outward, react with the oxygen from the atmosphere, and form an oxide scale [7,23]. The Al-depleted regions then tend to decompose, allowing for the formation of Cr-carbides, in this instance Cr₇C₃. Fig. 3(b) shows XRD data from the $24\text{--}36^{\circ}~2\theta$ range for which $\alpha\text{--}Al_2O_3$ peaks are identified. One can notice the asymmetric shape of the peaks but also the presence of what appears to be a second peak at approx. 34.7° for the SSR, RS.cb, RS.Cr₃C₂ samples. While it is less obvious in the case of the SSR sample, another contribution can also be seen at approx. 25.3°. The emergence of these peaks could indicate the presence of an isostructural (Al,Cr)2O3 solid solution, which can be expected considering that the Cr of the MAX phase and of the secondary phases oxidizes as well.

The behavior of the MS3 sample during oxidation was further investigated in order to detect the temperature at which the sample experiences weight gain, *i.e.* the formation of a scale. The first DSC signal of the MS3 sample oxidized up to $1100~^{\circ}$ C, in air at a heating rate of 20 $^{\circ}$ C/min is shown in Fig. 4, and allows identifying potential reactions that

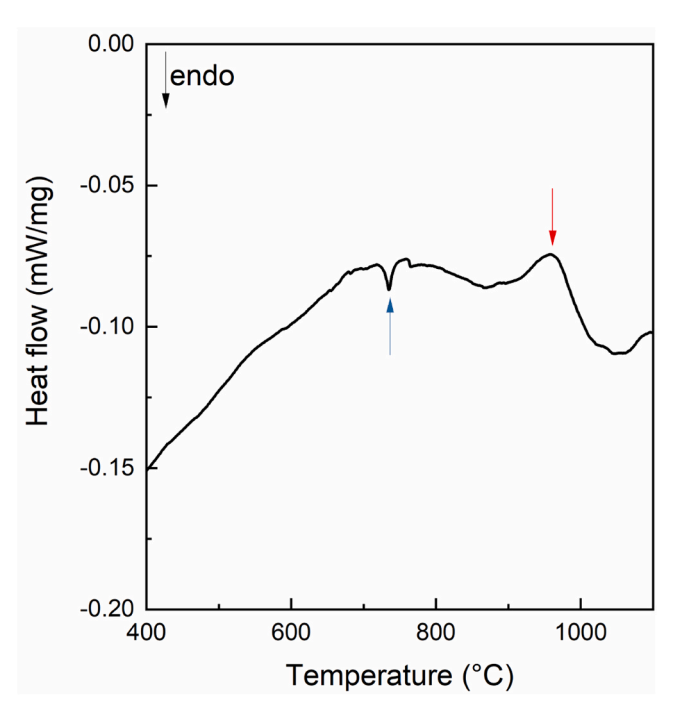


Fig. 4. DSC signal of the MS3 sample oxidized up to 1100 $^{\circ}\text{C}$ with a heating rate of 20 $^{\circ}\text{C/min},$ in air.

occurred during oxidation. The MS3 sample exhibited an endothermic peak at $\sim\!728~^\circ\text{C}$ (blue arrow) which could correspond to the melting of KBr (734 $^\circ\text{C}$), the salt used during synthesis. Therefore, one may assume that leftover salt was still present in the sample, which was evacuated simultaneously as the oxidation was progressing, suggesting that the salt played a role in the poor oxidation resistance of the MS3 sample. An exothermic peak starting at approx. 900 $^\circ\text{C}$ (red arrow) is observed, which we attribute to the beginning of oxidation, which is about 100 $^\circ\text{C}$ higher than the onset of oxidation reported by Lin et al. [23] but in good

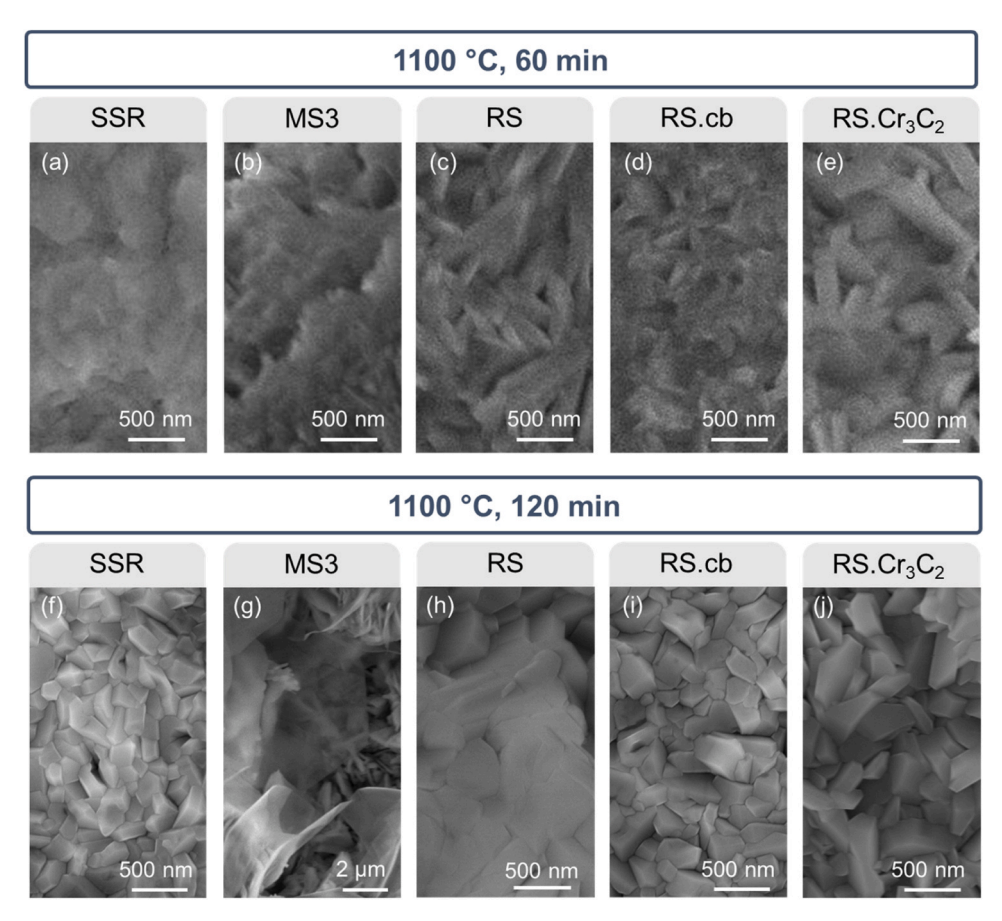


Fig. 5. Surface morphologies of Cr₂AlC samples oxidized at 1100 °C for (a)-(e) 60 min, and (f)-(j) 120 min.

agreement with observations made by Sharma and Pandey [13].

SEM micrographs of the top surfaces of the oxide scales formed on the Cr₂AlC samples oxidized at 1100 °C for 60 and 120 min, in air are shown in Fig. 5. The grain size of the oxide scales increases with increasing oxidation time. All oxide scale appearances, except that of the MS3 sample, are fairly similar, composed of somewhat elongated grains that are randomly oriented. The main differences between these oxide scales seems to be the roughness and presence of open porosities, as can be seen in Fig. 5 (c). The oxide scale of the MS3 sample seems to be mostly composed of sheet-like features (Fig. 5 (b) and (g)) which may suggest the formation of θ -Al₂O₃ prior to that of α -Al₂O₃ [24,25]. In fact, the rapid oxidation caused by the presence of leftover KBr in the MS3 sample could be responsible for the formation of the metastable θ -Al₂O₃.

Fig. 6 gathers the SEM cross-section micrographs of all samples after 60 min oxidation at 1100 $^{\circ}$ C, in air, and the HAADF STEM micrographs of samples oxidized for 120 min. Starting with 60 min oxidation time, the oxide scale of the SSR sample has a duplex-like structure (labeled with ox.1/ox.2). The top layer (ox.1) appeared to have more Cr than the bottom layer (ox.2), suggesting the formation of a (Cr,Al)₂O₃ mixed oxide (Fig. 6(a)). Adjacent to the scale, a thick Cr-carbide layer can be seen. The active consumption of the MS3 sample was confirmed, as no MAX phase was detected in the observed area (Fig. 6(b)). Instead, an inhomogeneous Al₂O₃ scale of varying thickness was detected on top of a highly porous Cr₇C₃ zone. The inhomogeneity of the scale leads to poor protection, which further enhances the oxidation of the MAX phase and its decomposition into carbides. The RS sample exhibits a continuous Al₂O₃ layer followed by discontinuous Cr-carbide-rich zones (Fig. 5(c)). Such observations would suggest that Al diffuses out of certain grains rather than others, which is most probably related to their orientation. No Cr-carbide was detected at the vicinity of the oxide scale in the RS.cb sample, as can be seen in Fig. 6(d) which we attributed to the excess Al

present in the as-sintered material (27.3 at%). Furthermore, the oxide scale exhibited a duplex structure similar to that of the SSR sample. Here as well, the top layer contained a certain amount of Cr, suggesting that the Cr available at the surface has oxidized at the same time as the Al. Finally, the RS.Cr₃C₂ sample also shows the formation of a duplex oxide scale, as can be seen in Fig. 6(e), in which the top oxide scale, contained more Cr than the bottom one, and appeared faceted and denser, while underneath the oxide, a thick Cr-carbide layer was observed.

The cross-section STEM micrograph of the MS3 sample, oxidized for 120 min (Fig. 6(g)), suggests that the MAX phase has fully decomposed, as EDX analyses confirmed the presence of a significant amount of Al_2O_3 at the surface and Cr-carbides. The remaining samples (Fig. 6(f), (h), (i), (j)) show the presence of an oxide scale, a Cr-carbide sublayer, and the remaining MAX phase. Even after longer oxidation, the SSR, RS.cb and RS.Cr₃C₂ exhibited duplex oxide scales, while the RS sample's oxide scale was homogeneous throughout and was accompanied by discontinuous Cr_7C_3 zones, similar to what was observed in Fig. 6. After 120 min oxidation, the RS.cb sample also exhibited thin Cr-carbide regions below the oxide scale, suggesting that the excess Al has been consumed and that Al has also diffused out of the MAX phase at the vicinity of the oxide scale.

Based on thermodynamic calculations reported in [12,18], the Cr-containing oxide scale likely forms because of the combination of elevated temperatures and the air mole fraction. The Cr_2O_3 formation is expected to be driven by the decomposition of Cr_7C_3 and therefore should be located at the interface between the oxide scale and the underlying material, as observed after 1000 h of oxidation of Cr_2AlC at 1000 °C [12]. However, this was not observed herein, most probably due to the short oxidation times used. Indeed, the Cr_2O_3 -containing oxide was found at the top of the oxide scale rather than at the interface with the Cr_2AlC . These observations suggest that the MAX phase and the

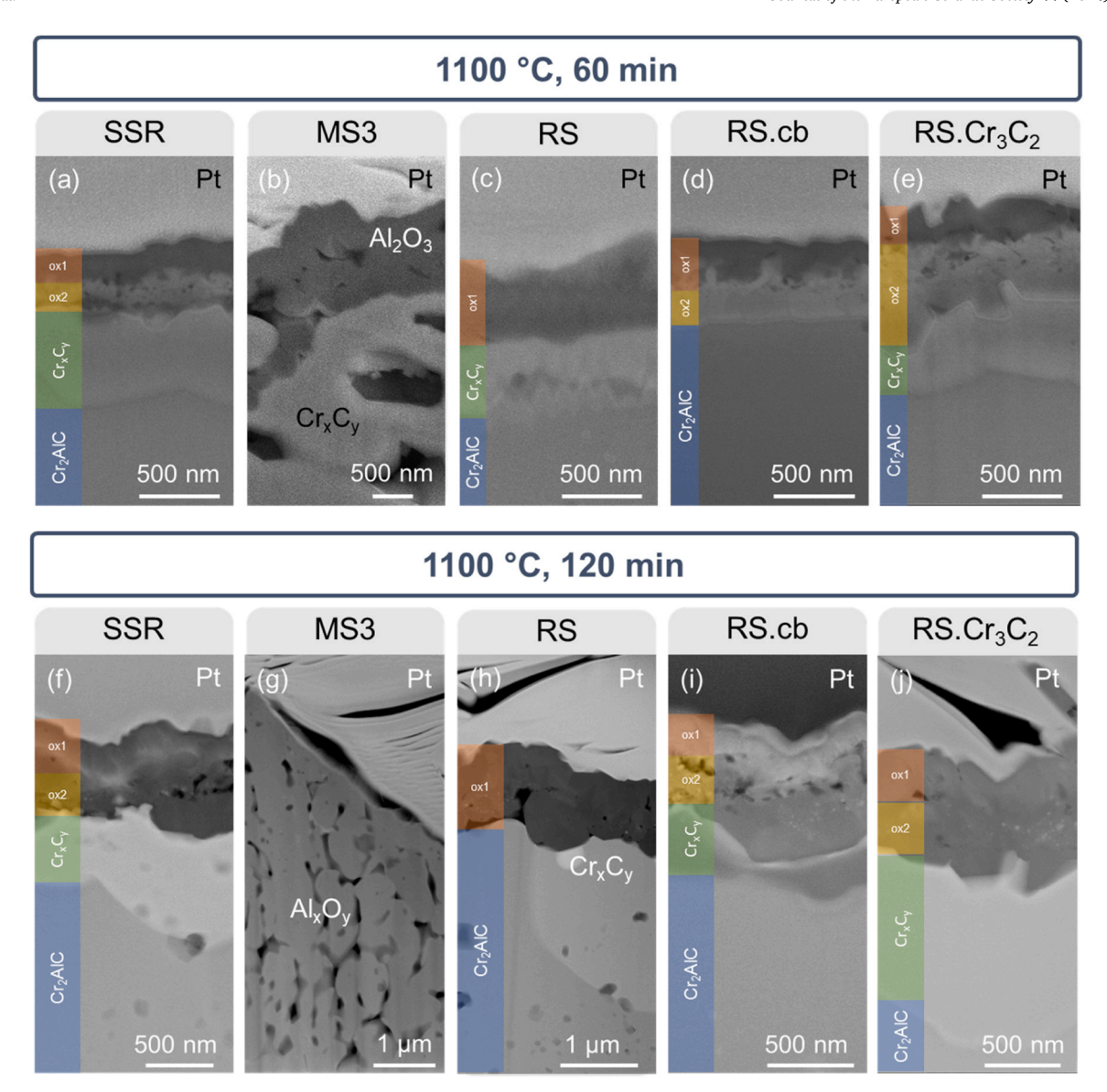


Fig. 6. (a)-(e) SEM cross-section micrographs (secondary electrons) of the Cr_2AlC samples oxidized at 1100 °C, for 60 min, and (f)-(j) HAADF STEM micrographs of thin lamellae extracted from Cr_2AlC samples oxidized at 1100 °C for 120 min.

Cr-containing impurities, Cr_7C_3 and $AlCr_2$ previously identified by Rietveld refinement, oxidize in similar time frames. In fact, it would appear that the secondary phases present may have a determinant role on the oxidation behavior of Cr_2AlC . Indeed, duplex oxide scales seem to have formed when $AlCr_2$ was identified in the as-sintered MAX phase. In fact, $AlCr_2$ is a metastable phase that tends to decompose into Al_3Cr and Cr [26]. In presence of an oxidizing environment, one may expect these intermetallics to oxidize into mixed $(Cr,Al)_2O_3$ oxides. Furthermore, the presence of Cr_7C_3 could also explain the presence of Cr in the oxide scale, as Cr-carbides present at the surface would oxidize as well.

The duplex oxide scales were observed in bright field STEM mode, as shown in Fig. 7. It can clearly be seen that the top oxide scales were much denser than the bottom ones in which pores were visible, particularly in the case of the SSR and RS.cb samples. The duplex structure was not as clear for the RS.Cr₃C₂ sample, although it was confirmed by EDX linescans (Fig. 7(d)), where Cr-enrichment was observed on the outermost surface. These Cr-enriched areas can also be seen on the EDX linescans of the SSR and RS.cb samples. Furthermore, based on the linescan of the RS.cb sample in Fig. 7(c) one may observe that the Aldepleted zone below the oxide scale contains close to 10 at% Al which is in contrast to observations made for the SSR sample, in which the Al

content decreased to nearly 0 at%. This observation suggests an increased diffusion of Al through the carbide/MAX phase region in the case of the RS.cb sample. This observation is in good agreement with observations made by Li *et al.* in which they compared the oxidation behavior of coarse and fine-grained Cr_2AlC [17]. A $Cr_2Al_{1-x}C$ zone was detected under the oxide scale in the case of the fine-grained sample, whereas Cr_7C_3 was detected beneath the oxide scale of the coarse-grained sample.

The RS sample exhibited a chemically homogeneous Al_2O_3 scale, made up of quasi-equiaxed grains, which seemed to have poor adhesion with the underlying MAX phase. Furthermore, one may notice the lack of a continuous Cr-carbide layer below the oxide scale but the presence of spherical and/or elongated carbide zones. As the SSR and RS samples have similar Cr:Al ratios (Table 3), one might expect similar oxide scale formation. However, that is not the case as the RS sample led to the formation of a homogeneous Al_2O_3 scale instead of the duplex scale observed on the SSR sample. Hence, this discrepancy could be due to the grain size difference between the two samples. In fact, although the average grain sizes extracted were 4.7 μ m for the SSR and 3.0 μ m for the RS sample, the RS sample contains a larger fraction of smaller (< 1 μ m) grains, which could contribute to an increased number of diffusion paths

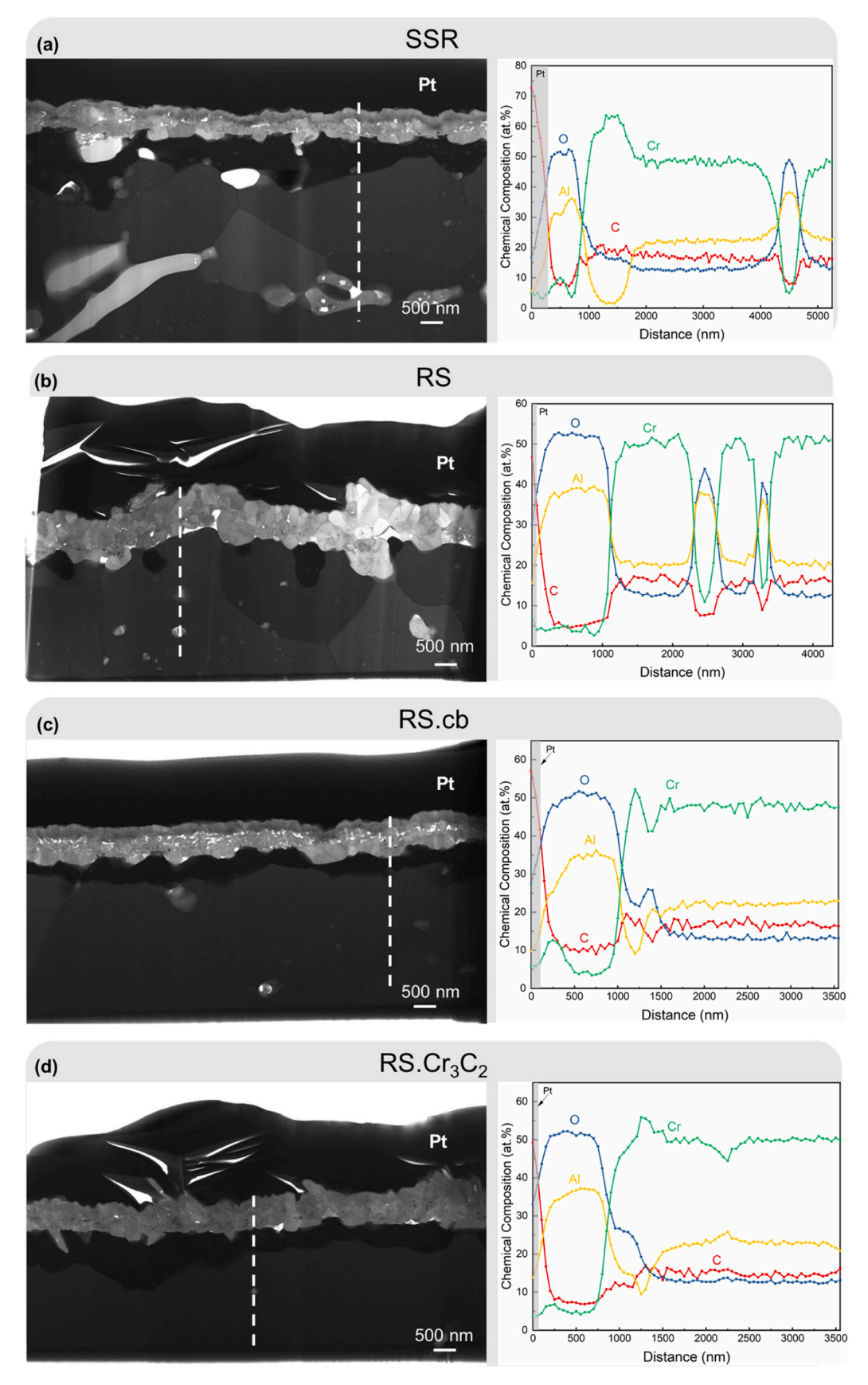


Fig. 7. Bright field STEM images of the cross-sections of the Cr_2AlC samples after 120 min oxidation at 1100 °C, in air, accompanied by EDX linescans.

Table 4 Oxide scale thicknesses of the Cr_2AlC samples after 60- and 120-min oxidation at 1100 °C, in air, measured from SEM cross-section micrographs.

Sample	Top oxide scale (nm)	Bottom oxide scale (nm)	Cr-carbide (nm)
SSR – 60 min	246 ± 43	318 ± 75	545 ± 213
SSR - 120 min	219 ± 24	389 ± 88	595 ± 213
MS3 - 60 min	1232 ± 408	-	-
MS3 - 120 min	-	-	-
RS - 60 min	754 ± 150	-	469 ± 188
RS - 120 min	1028 ± 227	-	$599\pm283^{\text{a}}$
RS.cb - 60 min	273 ± 57	290 ± 81	-
RS.cb - 120 min	217 ± 49	491 ± 90	468 ± 151
RS.Cr ₃ C ₂ – 60 min	295 ± 78	454 ± 131	583 ± 279
RS.Cr ₃ C ₂ – 120 min	Combined 772 \pm 1	57	454 ± 172

^a discontinuous Cr-carbide zones instead of continuous layer

for Al species.

The oxide scale thicknesses measured on the samples oxidized for 60 and 120 min are summarized in Table 4. The thickest oxide scale was detected on the MS3 sample oxidized for 60 min. The sample was excluded from the discussion for longer oxidation times because of its decomposition upon oxidation. The RS.Cr₃C₂ sample exhibited the thickest duplex oxide scale combined with an approx. 600 nm-thick carbide layer after 60 min, indicating that the protectiveness of the top oxide scale was not sufficient to hinder the inward O²⁻ diffusion and the consumption of Al diffusing from the volume of the sample. Both SSR and RS.cb samples exhibited similar duplex oxide scale thicknesses. However, the SSR sample exhibited an approx. 550 nm-thick carbide layer, whereas the RS.cb sample did not, suggesting that the Al is not diffusing in the same way. In fact, the absence of Cr-carbide scale in the case of the RS.cb sample can be threefold. First, the Al content was higher in the RS.cb sample, suggesting that mobile Al is able to diffuse and oxidize at the surface without decomposing the MAX phase into carbides. Second, based on the average grain size reported in Fig. 2, the RS.cb sample contains more grain boundaries, which serve as diffusion paths for both O²⁻ and Al³⁺ species. The increased number of diffusion paths can allow for Al from the volume of the sample to diffuse to the Aldepleted zones below the oxide scale, while in the case of SSR, the Al from the volume can only take longer diffusion paths. Third, the submicron grains, being highly energetic because of their small size, can provoke microstructural evolution by growth and/or coalescence of grains during the oxidation process. Therefore, three causes that enabled Al replenishment close to the oxide/MAX phase interface were identified: (i) the presence of free Al (in the form of AlCr₂ or metallic Al), (ii) grain boundary diffusion, and (iii) grain growth/coalescence.

As expected, the oxide scale thicknesses increased with increasing oxidation time, from 60 to 120 min. While the oxide scale of the SSR sample was the thinnest (approx. 608 nm, combined), the carbide layer itself was thicker (approx. 595 nm) than those of the RS.Cr₃C₂ (approx. 454 nm) and RS.cb (approx. 468 nm) samples. The oxide scale of the RS sample was thicker than the other samples (approx. 1028 nm), but the lack of a continuous Cr-carbide layer suggests that oxygen does not diffuse through the scale with much ease. This is supported by the relatively dense microstructure of the oxide scale seen in Fig. 7(b), despite its poor adhesion at the oxide/MAX phase interface. The thicknesses of the top oxide scales don't seem to increase significantly between 60 and 120 min, as seen from the values reported in Table 4. However, the bottom oxide scale of the RS.cb sample has almost doubled, and Cr-carbide was observed. This suggests that Al from the MAX phase has started diffusing, leading to the decomposition of the MAX phase into carbides. Furthermore, the increased thickness of the RS.cb bottom oxide scale compared to that of the SSR sample also suggests enhanced Al diffusion from the volume of the RS.cb sample. As for the RS.Cr₃C₂ sample, it was difficult to differentiate the top from the

bottom oxide scale. However, based on the EDX linescan in Fig. 7, the presence of Cr on the outermost surface confirms that the oxide scale is still duplex-like after 120 min of oxidation.

4. Conclusions

In this work we investigated the effect of different processing routes and precursors on the formation of Cr_2AlC MAX phase using FAST/SPS. We show that highly dense Cr_2AlC samples can be produced using premade Cr_2AlC utilizing the SSR and MS3 processes. We also show that microstructural design of reactively sintered Cr_2AlC samples by varying the carbon source (graphite vs. carbon black vs. Cr_3C_2) is possible. Indeed, the smallest grain sizes were obtained for the RS.cb sample in which the carbon source was nanometric. As the carbon source increased in grain size, the average grain size of the MAX phase increased as well.

We further investigated the oxidation behavior of the produced Cr₂AlC specimens at 1100 °C for 60 and 120 min, in air. MS3 did not sustain the oxidation treatment because of leftover KBr used during the synthesis process and the growth of a non-protective Al₂O₃ scale, which accelerated the oxidation, as supported by DSC, XRD, and microstructural observations. The RS sample was the only sample exhibiting the formation of a quasi-pure Al₂O₃ scale. This scale was not followed by a homogeneous Cr-carbide layer but rather by discontinuous Cr-carbiderich zones/grains, which could be linked to the preferential diffusion paths for Al that relate to grain orientation. The remaining samples exhibited duplex-like oxide scales, where the top layer contained up to approx. 12 at% of Cr, making it a mixed (Cr,Al)2O3 oxide, which was associated with the presence of Cr-containing secondary phases (Cr₇C₃ and AlCr₂). The bottom layer appeared to be primarily Al-rich. The assintered composition of the Cr2AlC samples appear to play a role in the formation of Cr-carbides below the oxide scale. In fact, based on observations made on the RS.cb sample, three causes were identified that may have contributed to the absence of a Cr-carbide layer after 60 min oxidation at 1100 $^{\circ}$ C. First, the as-sintered sample had excess Al either as enriched Cr2AlC grains or in the form of AlCr2, second, its grain size was the smallest, which led to numerous diffusion paths, and third, the sample underwent microstructural evolution during oxidation, which allowed the redistribution of Al in the MAX phase.

CRediT authorship contribution statement

Clio Azina: Conceptualization, Methodology, Validation, Formal analysis, Investigation, Data curation, Writing Original Draft, Visualization, Project administration, funding acquisition. Melina Poll: Investigation, Writing Review & Editing. Damian M. Holzapfel: Investigation, Writing Review & Editing. Elodie Tailleur: Validation, Formal analysis, Investigation, Resources, Writing Review & Editing. Axel Zuber: Investigation, Formal analysis, Writing Review & Editing. Sylvain Dubois: Writing Review & Editing, Supervision, Funding acquisition. Per Eklund: Writing Review & Editing, Supervision. Jesus Gonzalez-Julian: Methodology, Validation, Resources, Writing Review & Editing, Supervision, Project administration.

Declaration of Competing Interest

The authors declare that they have no known competing financial interests or personal relationships that could have appeared to influence the work reported in this paper.

Acknowledgements

C. A. gratefully acknowledges funding from the European Union's H2020-MSCA-IF-2019 research and innovation programme under the Marie Curie grant agreement No. 892501 (REALMAX). E. T. acknowledges the PMD²X X-ray diffraction facility of the CRM² laboratory,

Université de Lorraine, for X-ray diffraction measurements: https://cr m2.univ-lorraine.fr/plateformes/pmd2x). A. Z. and S. D. acknowledge the Région Nouvelle-Aquitaine, the Ministère de l'Enseignement Supérieur et de la Recherche and the French government program "Investissements d'Avenir" (EUR INTREE, reference ANR-18-EURE-0010 and LABEX INTERACTIFS, reference ANR-11-LABEX-0017-01).

References

- M.W. Barsoum, T. El-Raghy, The MAX phases: Unique new carbide and nitride materials, Am. Sci. 89 (2001) 334–343, https://doi.org/10.1511/2001.4.334.
- [2] P. Eklund, M. Beckers, U. Jansson, H. Högberg, L. Hultman, The Mn + 1AXn phases: Materials science and thin-film processing, Thin Solid Films 518 (2010) 1851–1878, https://doi.org/10.1016/j.tsf.2009.07.184.
- [3] M.W. Barsoum, M. Radovic, Elastic and Mechanical Properties of the MAX Phases, Annu. Rev. Mater. Res. (2011), https://doi.org/10.1146/annurev-matsci-062910-100448
- [4] C. Azina, S. Mráz, G. Greczynski, M. Hans, D. Primetzhofer, J.M. Schneider, P. Eklund, Oxidation behaviour of V2AlC MAX phase coatings, J. Eur. Ceram. Soc. 40 (2020) 4436–4444, https://doi.org/10.1016/j.jeurceramsoc.2020.05.080.
- [5] S. Badie, D. Sebold, R. Vaßen, O. Guillon, J. Gonzalez-Julian, Mechanism for breakaway oxidation of the Ti2AlC MAX phase, Acta Mater. 215 (2021), https://doi.org/10.1016/j.actamat.2021.117025.
- [6] J. Gonzalez-Julian, Processing of MAX phases: From synthesis to applications, J. Am. Ceram. Soc. 104 (2021) 659–690, https://doi.org/10.1111/jace.17544.
- [7] D.E. Hajas, M. To Baben, B. Hallstedt, R. Iskandar, J. Mayer, J.M. Schneider, Oxidation of Cr2AIC coatings in the temperature range of 1230 to 1410°C, Surf. Coat. Technol. 206 (2011) 591–598, https://doi.org/10.1016/j. surfcoat.2011.03.086.
- [8] B. Cui, W.E. Lee, B. Cui, W.E. Lee, High-temperature Oxidation Behaviour of MAX Phase Ceramics, Refract. World 5 (2013) 105–112.
- [9] M. Fekete, C. Azina, P. Ondračka, L. Löfler, D. Bogdanovski, D. Primetzhofer, M. Hans, J.M. Schneider, On the determination of the thermal shock parameter of MAX phases: a combined experimental-computational study, J. Eur. Ceram. Soc. (2023) S0955221923003679, https://doi.org/10.1016/j. jeurceramsoc.2023.05.007.
- [10] C. Azina, S. Badie, A. Litnovsky, L. Silvestroni, E. Sani, J. Gonzalez-Julian, Optical properties and corrosion resistance of Ti2AlC, Ti3AlC2, and Cr2AlC as candidates for concentrated solar power receivers, Sol. Energy Mater. Sol. Cells 259 (2023) 112433, https://doi.org/10.1016/j.solmat.2023.112433.
- [11] B. Cui, D.D. Jayaseelan, W.E. Lee, TEM study of the early stages of Ti 2AlC oxidation at 900 °c, Scr. Mater. 67 (2012) 830–833, https://doi.org/10.1016/j.scriptamat.2012.07.045.
- [12] A. Zuber, V. Gauthier-Brunet, J. Roger, J. Gonzalez-Julian, T. Ouisse, S. Dubois, Cr2AlC high temperature oxidation under dry and wet air: understanding of the oxidation mechanism, J. Eur. Ceram. Soc. (2023), https://doi.org/10.1016/j. jeurceramsoc.2023.05.012.

- [13] P. Sharma, O.P. Pandey, Non-isothermal oxidation kinetics of nano-laminated Cr 2 AlC MAX phase, J. Alloy. Compd. 773 (2019) 872–882, https://doi.org/10.1016/j. iallcom.2018.09.326.
- [14] Z. Wang, G. Ma, L. Liu, L. Wang, P. Ke, Q. Xue, A. Wang, High-performance Cr2AlC MAX phase coatings: Oxidation mechanisms in the 900–1100°C temperature range, Corros. Sci. 167 (2020) 108492, https://doi.org/10.1016/j.corsci.2020.108492.
- [15] L. Shang, K.G. Pradeep, S. Sandlöbes, M. to Baben, J.M. Schneider, Effect of Si additions on the Al 2 O 3 grain refinement upon oxidation of Cr 2 AlC MAX phase, J. Eur. Ceram. Soc. 37 (2017) 1339–1347, https://doi.org/10.1016/j.jeurceramsoc.2016.11.050.
- [16] K.G. Pradeep, K. Chang, A. Kovács, S. Sen, A. Marshal, R. de Kloe, R.E. Dunin-Borkowski, J.M. Schneider, Nano-scale Si segregation and precipitation in Cr 2 Al (Si)C MAX phase coatings impeding grain growth during oxidation, Mater. Res. Lett. 7 (2019) 180–187, https://doi.org/10.1080/21663831.2019.1572663.
- [17] S. Li, X. Chen, Y. Zhou, G. Song, Influence of grain size on high temperature oxidation behavior of Cr 2AlC ceramics, Ceram. Int. 39 (2013) 2715–2721, https:// doi.org/10.1016/j.ceramint.2012.09.039.
- [18] A. Zuber, V. Gauthier-Brunet, J. Roger, J. Gonzalez-Julian, T. Ouisse, S. Dubois, Towards a better understanding of the high-temperature oxidation of MAX phase Cr2AlC, J. Eur. Ceram. Soc. 42 (2022) 2089–2096, https://doi.org/10.1016/j. ieurceramsoc.2021.12.057.
- [19] J. Gonzalez-Julian, S. Onrubia, M. Bram, O. Guillon, Effect of sintering method on the microstructure of pure Cr2AlC MAX phase ceramics, J. Ceram. Soc. Jpn. 124 (2016) 415–420, https://doi.org/10.2109/jcersj2.15263.
- [20] A. Dash, R. Vaßen, O. Guillon, J. Gonzalez-Julian, Molten salt shielded synthesis of oxidation prone materials in air, Nat. Mater. 18 (2019) 465–470, https://doi.org/ 10.1038/s41563-019-0328-1.
- [21] J. Rodríguez-Carvajal, Recent advances in magnetic structure determination by neutron powder diffraction, Phys. B: Condens. Matter 192 (1993) 55–69, https://doi.org/10.1016/0921-4526(93)90108-I.
- [22] A. Dash, Y.J. Sohn, R. Vaßen, O. Guillon, J. Gonzalez-Julian, Synthesis of Ti3SiC2 MAX phase powder by a molten salt shielded synthesis (MS3) method in air, J. Eur. Ceram. Soc. 39 (2019) 3651–3659, https://doi.org/10.1016/j.jeurceramsoc.2019.05.011.
- [23] Z.J. Lin, M.S. Li, J.Y. Wang, Y.C. Zhou, High-temperature oxidation and hot corrosion of Cr2AlC, Acta Mater. 55 (2007) 6182–6191, https://doi.org/10.1016/j. actamat.2007.07.024.
- [24] V.K. Tolpygo, D.R. Clarke, Microstructural study of the theta-alpha transformation in alumina scales formed on nickel-aluminides, Mater. High. Temp. 17 (2000) 59–70. https://doi.org/10.1179/mht.2000.011.
- [25] D.B. Lee, T.D. Nguyen, S.W. Park, Long-Time Oxidation of Cr2AlC between 700 and 1,000 °c in Air, Oxid. Met. 77 (2012) 275–287, https://doi.org/10.1007/s11085-012-9285-7.
- [26] Materials Data on AlCr2 by Materials Project, Lawrence Berkeley National Lab. (LBNL), Berkeley, CA (United States). LBNL Materials Project, 2020. (https://doi.org/10.17188/1192273).